Volume 17, Number 2, 2024. pp. 233-244

Jordan Journal of Physics

ARTICLE

Determination of Crystallographic Information by Means of Very Low Energy Electron Imaging

Zuzana Pokorná[a], **Alexandr Knápek**[a], **Filip Mika**[a], **Jana Chlumská**[a], **Ivo Konvalina**[a], **Christopher G.H. Walker**[b] and **Ahmad M. D. (Assa'd) Jaber**[c]

[a] *Institute of Scientific Instruments, Czech Academy of Sciences, Královopolská 147, Brno, 612 64, Czech Republic.*

[b] *Department of Electronics, University of York, Heslington, York, North Yorkshire, YO10 5DD, UK.*

[c] *Departement of Basic Medical Sciences, Faculty of Medicine, Aqaba Medical Sciences University, Ports Hwy, Aqaba, 77110, Jordan.*

Doi: **https://doi.org/10.47011/17.2.10**

Received on: 15/02/2023; *Accepted on: 30/10/2023*

Abstract: The present work explores the possibility of using scanning low energy electron microscopy (SLEEM) to obtain crystallographic orientation information from the variation in very low energy (0-50 eV) electron reflectivity. SLEEM is a scanning microscopy technique that allows imaging with electrons at arbitrarily low incident energies while preserving very good image resolution. As the incident electron energy changes in the very low energy range of tens of eV and less, the image signal of reflected electrons varies. Since the reflectivity of very low energy electrons in the range of 0–30 eV correlates with the crystal structure normal to the surface of the material, it can be used to determine the crystallographic orientation with nanoscale resolution.

Keywords: SLEEM, LEEM, Very low energy electrons, Crystallographic orientation.

1. Introduction

The theoretical analysis of experimental spectra in secondary electron emission spectroscopy (SEES), target-current spectroscopy (TCS), and low-energy electron transmission (LEET) is challenging due to the need to account for all electron scattering processes within crystals. Surface cleanliness is of crucial [1] and surface adsorbates significantly alter the spectra [2]. This can be used for sensitive observation of adlayer buildup or epitaxial growth, especially in low-energy electron microscopy (LEEM) [3-5].

Low-energy electron diffraction (LEED) and LEEM are related techniques where a beam of low-energy electrons (10 to 100 eV) interacts with a sample surface, being mostly elastically backscattered and diffracted. LEED, or very-low-energy electron diffraction (VLEED) at the lowest energy range, focuses on the electron diffraction pattern of a single location on the sample. However, LEEM uses signals from particular diffraction spots to generate surface images. Surface roughness significantly influences the density of states [6-10]. Surface resonances may appear in reflectivity spectra [11], overlapping with bulk features.

Scanning low-energy electron microscopy (SLEEM) is useful for examining various

Corresponding Author: Alexandr Knápek **Email**: knapek@isibrno.cz

materials, enhancing image parameters, such as crystallographic and atomic number contrast [12]. The main advantage of SLEEM is that it offers high collection efficiency by collimating and accelerating most signal electrons towards the detector.

The present work demonstrates the application of SLEEM to obtain crystallographic orientation information for the copper and aluminum polycrystalline samples from the variation of very-low-energy (0-50 eV) electron reflectivity. Throughout this paper, the term “electron reflectivity” is used for brevity, although the signal contains both elastically and inelastically reflected electrons, as well as secondary electrons.

2. Experimental Setup

2.1. Scanning Low Energy Electron Microscope (SLEEM)

Scanning low energy electron microscopy (SLEEM) is a scanning electron microscope (SEM) technique that allows using arbitrarily low electron energies while preserving very good image resolution [4, 13] by making use of a cathode lens [14]. A cathode lens is an immersion electrostatic lens inserted between the sample and the last lens of a conventional SEM, decelerating electrons from their primary energy E_{prim} to a chosen incident energy E_{inc} just before they hit the sample. A cathode lens essentially takes the form of a negatively biased sample and a grounded backscattered electron (BSE) detector above it. The incident electron energy E_{inc} can be chosen arbitrarily by setting the negative sample bias U_{bias}, where $E_{inc} = E_{prim} - |e \cdot U_{bias}|$.

The length of the cathode lens decelerating field (distance between the negatively biased sample and the grounded BSE detector) is 5 mm in standard configurations. The working distance (WD), or the distance between the objective lens nozzle and the sample, is 8 mm. Figure 1 shows a schematic sketch of a cathode lens.

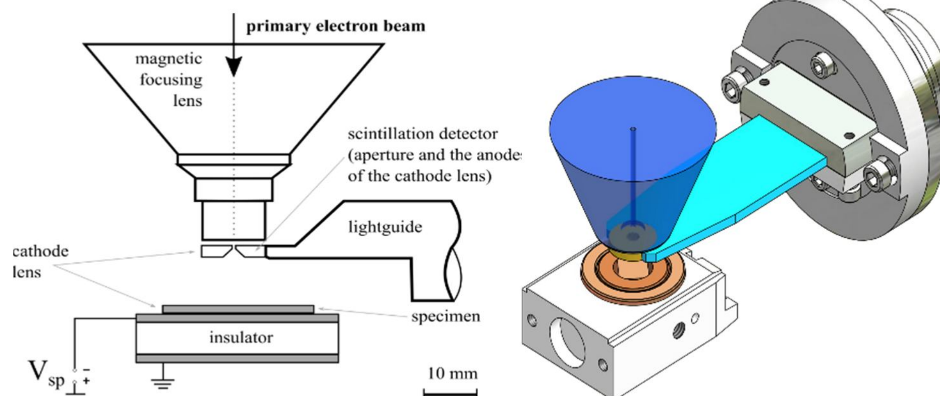

FIG. 1. The schematic diagram of a cathode lens (adapted from [15]). Under the nozzle of the objective lens of the scanning electron microscope (blue cone) is the annular BSE detector (yellow disk) set in a flat light guide (light blue). Below is the sample holder covered by a flat conductive cap (orange circle).

The experiments were performed in the Tescan Vega TS 5130MM ultra-high vacuum scanning low energy electron microscope manufactured by the Tescan Company in 2004. The UHV SLEEM-III is a non-commercial scanning electron microscope of an in-house design, working in the ultra-high vacuum pressure range and equipped for SLEEM. Ultra-high vacuum conditions ($P = 10^{-8}$ Pa) are necessary because otherwise there is a strong influence of adlayers adsorbed on the surface on the resulting reflectivity. While pristine cleanliness of the surface is admittedly a restrictive experimental requirement, it also allows for assessing the presence and influence of adsorbates (surface reconstruction, growth of layers, etc.) on the sample surface. Figure 2 illustrates the influence of adsorbed layers on the surface of a polycrystalline copper sample, showing how the signal from the bright oxide overlayer differs from the signal from the polycrystalline bulk. This difference is marked throughout the entire 0-30 eV range of incident energies.

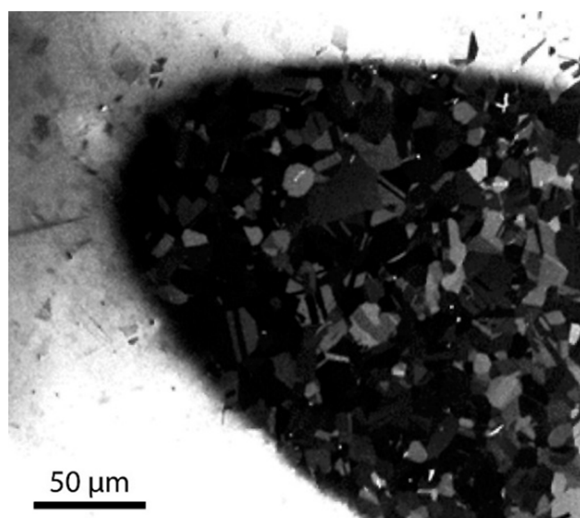

FIG. 2. The dark oval shape of a sputtered-off surface oxide revealing the polycrystalline bulk underneath imaged at 5 keV primary energy and 1 keV incident electron energy, using the cathode lens.

The main ultra-high vacuum chamber of the UHV SLEEM-III houses a sample holder that can apply a negative voltage bias to the sample. The holder is also equipped with sample manipulators allowing for tilting, rotation, and shifting in three axes. Signals from the sample can be detected by a scintillation detector of back-scattered electrons mounted above the sample, which also serves as the grounded electrode in the cathode lens arrangement. The UHV SLEEM-III includes a preparation chamber equipped for *in situ* cleaning through ion sputtering and electron bombardment heating. The base pressure in this chamber is maintained in the range of 10^{-7} Pa range.

While the SLEEM arrangement is very advantageous in terms of preserving the lateral resolution, the present experiment setup also introduces several artifacts, such as variability of the angle of incidence with incident energy and the apparent limitation of the field of view at the lowest energies. The influence of these artifacts on resulting images is discussed further in this article.

2.2. Samples and Sample Preparation

The polycrystalline samples chosen were copper and aluminum, polished and etched to obtain a smooth surface, and then annealed for an extended period to eliminate any residual stresses. The single crystals, also copper and aluminum, were oriented along the three basic planes: (100), (110), and (111). These crystals were obtained from MaTecK GmbH. Each sample was cleaned *ex situ* with chemical solvents and then further cleaned *in situ* through several cycles of ion sputtering alternating with electron bombardment heating [16]. All samples were rinsed in methyl alcohol prior to their insertion into the preparatory chamber. The samples were electrolytically cleaned in an aqueous mixture of ethyl alcohol, ether, and perchloric acid.

The samples were cleaned by at least three cycles consisting of 30 minutes of sputtering with 1 keV argon ions at a beam current of about 30 nA and an incidence angle of 5°. Sputtering was then followed by electron bombardment of the backside of the sample with 1500 eV electrons, which resulted in heating the sample to 400° C, as verified by a contactless infrared thermometer. In some cases, when contamination persisted, the target temperature was raised to 450° C for 75 seconds. The pressure rose to about 3×10^{-6} Pa during sample heating and to 1×10^{-5} Pa during ion sputtering. The final cleanliness of the sample was verified by Auger electron spectroscopy (AES). The AES spectrum, shown in Fig. 3, confirms the absence of oxides or hydrocarbons, revealing only the presence of bulk copper material.

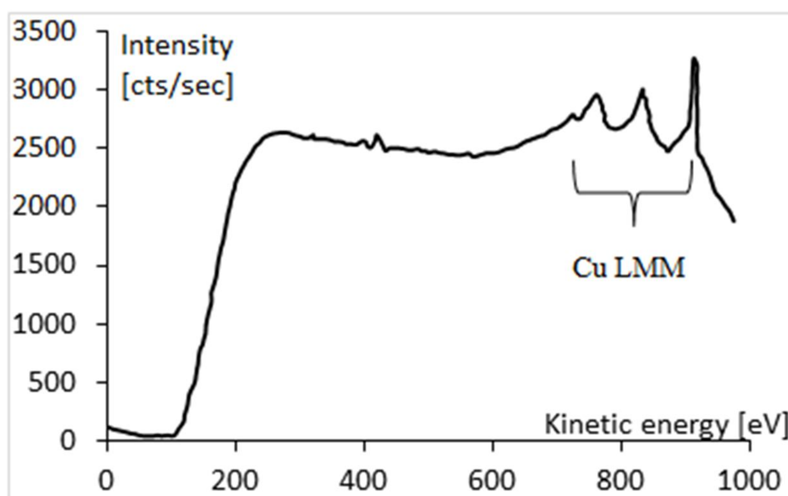

FIG. 3. Auger spectroscopy of the sputtered surface confirms the absence of oxides or hydrocarbons, revealing only the presence of bulk copper material.

2.3. The Set-up of a Typical Experiment

An ex situ-cleaned single crystal or polycrystalline sample is inserted into the airlock, pumped down into the high-vacuum (10^{-6} Pa) range, and then transferred with a vacuum manipulator into the ultra-high vacuum (10^{-7} Pa) preparation chamber for in situ cleaning. After cleaning, it is transferred to the main UHV (10^{-8} Pa) chamber. Once the cleanliness of the sample is verified by Auger electron spectroscopy, the sample position is adjusted so that its surface is normal to the incident electron beam. In the ideal case, the beam would be perfectly perpendicular to the surface of both the sample and the BSE detector acting as a counter-electrode, and perfectly parallel to the optical axis. However, the experimental setup can be affected by an alignment error that can amount to as much as 0.5°. After the alignment procedure, a series of images are taken at a preset range of incident electron energies (i.e. negative sample bias voltages). The energy range typically goes from 0 eV to a few tens of eV, in 0.3 eV steps.

Dedicated software is used for data acquisition, controlling automated bias increase and subsequent image data acquisition, as well as post-processing and evaluation of the obtained image series. This software also uses optimized image recognition procedures for discerning particular grains in a polycrystalline sample to attribute each measured reflectivity curve to each of the multitudes of grains. Several image series were also taken at larger and smaller working distances to evaluate the influence of the strength of the decelerating electrostatic field on the observed phenomena.

An important parameter influencing the signal collection efficiency is the diameter of the aperture through which the primary beam enters the cathode decelerating region, in other words, the diameter of the bore in the scintillating single crystal in the BSE detector, as seen in Fig. 1. In the present experiment, the bore's diameter is 300 µm, limiting the field of view to about 700 µm at the standard working distance of 8 mm.

The efficiency of collecting signal electrons in SLEEM is affected by the detection arrangement in which signal electrons leaving the sample are accelerated back to the scintillation detector. Electrons with a small component of the velocity parallel to the sample can only travel a short distance parallel to the sample before they hit the detector. If they are emitted near the optical axis, they end up in the detector bore and are lost for detection. Such is the case for signal electrons emitted at very low energy (Fig. 4). When the decelerated electron beam has but a few electron volts, a large portion of signal electrons emitted near the optical axis is lost, resulting in a darker circular area in the center of the SLEEM image, as illustrated in Fig. 5.

As shown in Fig. 4, the BSE bore unfortunately also permits some of the signal electrons to escape, decreasing the collection efficiency of very-low-energy electrons at high immersion ratios E_{prim}/E_{inc}. This issue should be addressed in the next UHV SLEEM model in which the entire bunch of signal electrons will be deflected off-axis to a detector.

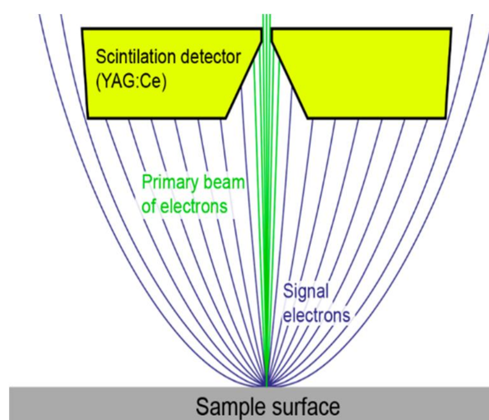

FIG. 4. At high immersion ratios E_{prim}/E_{inc} = 120, with E_{prim} = 6 keV and E_{inc} = 50 eV, the trajectories of very low energy signal electrons are drawn into a very tight pencil even though they escape the sample at all possible angles. Signal electrons emerging from areas near the center of the field of view escape through the BSE detector bore and are lost for detection, causing a decrease in the collection efficiency at the lowest incident energies [15].

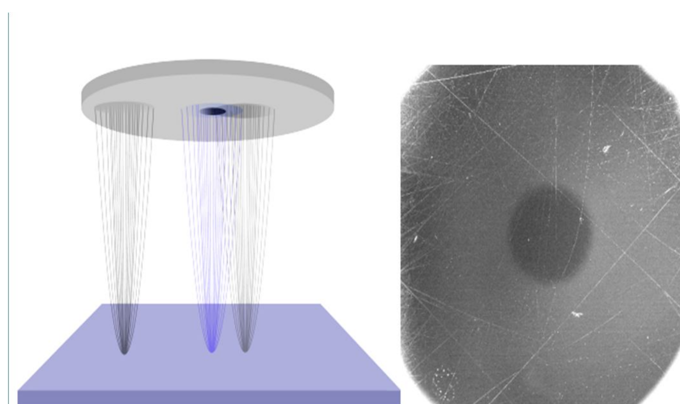

FIG. 5. Deteriorated collection efficiency near the image center at high immersion ratios. On the right, a high-gain image exhibits an uneven brightness due to signal loss in the detector bore.

A slight defocus of the image reveals concentric circles around the dark spots, suggesting that the dark spots are multiple images of the opening of the objective lens nozzle, along with the machined ridges. This seems to be caused by some part of the emitted signal being lost in the detector bore, either by certain angle ranges (angular anisotropy of the reflected signal) or by certain energy ranges. Electrons with the lowest energies drawn toward the detector are the strongest, and their entire angular distribution is drawn into only a thin pencil (Fig. 6).

The angle of incidence α_{inc} of the decelerated primary beam on the sample is an important parameter co-determining the channeling pattern. In the present experiment, however, this angle varies with the distance from the center of the field of view, depending on the strength of the decelerating field $E=U/d$. This means that for a particular beam scan angle, the angle of incidence increases with negative sample bias U_{bias}, which corresponds to decreasing incident energy E_{inc}. A comparison of different angles of incidence for E_{inc}= 0.5, 10 eV, 30 eV, and 100 eV in otherwise identical conditions is shown in Fig. 6. As the field gets stronger, the angle of incidence increases to 90° for the lowest incident energies. This effectively means that the beam just grazes the surface or even turns back before it reaches the surface, resulting in an apparent field-of-view limitation, where the observable area around the center of the field of view becomes smaller (Fig. 7).

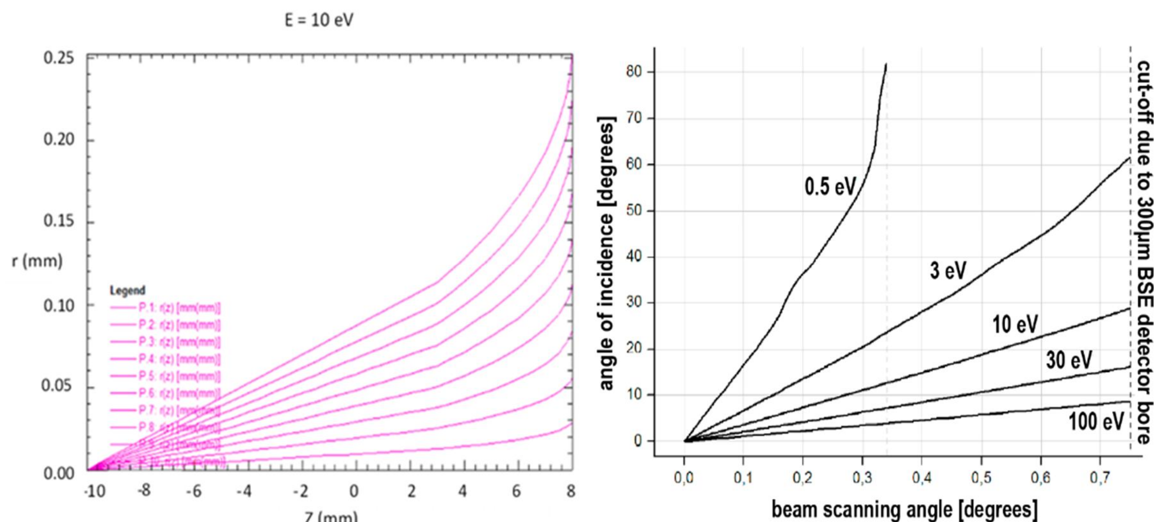

FIG. 6. *Left:* An example of the curved trajectories of decelerated beams for a standard set of conditions and E_{inc} = 10 eV. The scanning angle is varied in several steps between 0° and 0.5° which realistically corresponds to the entire field of view allowed by the hole in the BSE detector. *Right:* A comparison of different angles of incidence for a range of incident electron energies between E_{inc}= 0.5 eV and 100 eV.

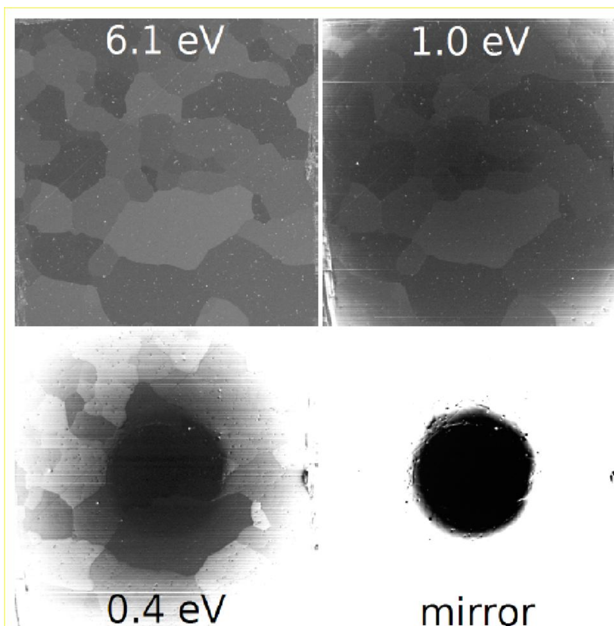

FIG. 7. An example of field-of-view limitation at the lowest incident energies. Sample: polycrystalline aluminum; UHV conditions

3. Experimental Results

In the incident energy range of 0–30 eV, the image of a Cu single crystal sample surface exhibits an overlay of fuzzy but regular patterns of varying brightness, as shown in Figs. 8–10. In addition to these patterns, circular dark spots can be seen in the image. These spots change their apparent brightness with energy but remain constant in size and position.

Images of polycrystalline samples appear to consist of partial images overlaid on each particular grain; these partial images correspond to parts of images taken from respective single crystal samples. For example, images of polycrystalline grains with an orientation close to (111) appear to be parts of a (111) single crystal image, as shown in Fig. 8.

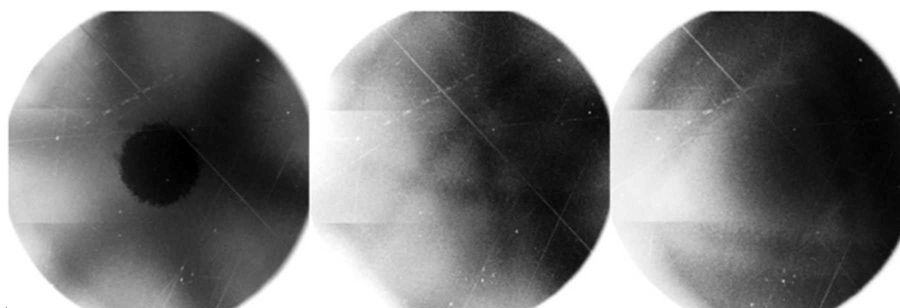

FIG. 8. A very-low-energy electron reflectivity image of a (111) fcc single crystal of Cu taken at the primary beam energy of 5020 eV and incident electron energies of 25.4 eV, 32.4 eV, and 38.4 eV, respectively. The patterns exhibit a distinct three-fold symmetry.

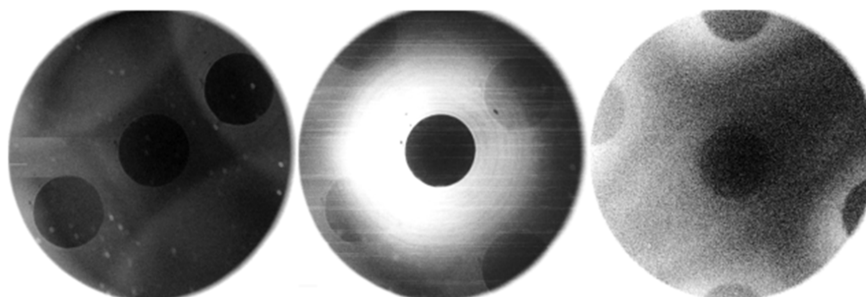

FIG. 9. Very-low-energy electron reflectivity images of a (110) fcc single crystal of Cu taken at the primary beam energy of 6020 eV and incident electron energies of 10 eV, 14 eV, and 23 eV, respectively. The dark spots exhibit a distinct rectangular spacing.

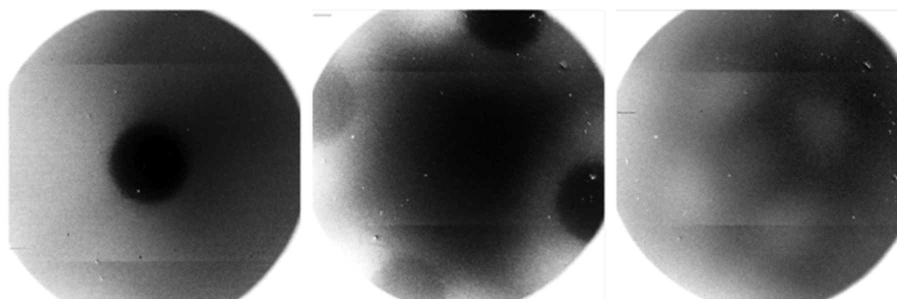

FIG. 10. A very-low-energy electron reflectivity image of a (100) fcc single crystal of Cu taken at the primary beam energy of 6020 eV and incident electron energies of 3 eV, 22 eV, and 29 eV, respectively. The patterns exhibit a distinct four-fold symmetry.

The regular geometric pattern formed by these dark spots exhibits the same symmetry as the crystal surface: an ordered square pattern for fcc (100), rectangular for fcc (110), and triangular for fcc (111). This suggests that the origin of these phenomena is related to crystalline structure.

The dark circular regions become smaller and move outward with increasing working distance (decreasing field strength). Their intensity changes with E_{inc}, but their position does not. If the energy of the primary beam changes but all other parameters remain the same, the resulting situation suggests that the cause is related to electron channeling and the electron structure.

3.1. Diffuse Patterns

The diffuse patterns with varying brightness are either linear or parts of circles. Their intensity and positions change with E_{inc} and become less pronounced with increasing working distance. Their symmetry is four-fold for a (100) fcc face, six-fold for a (111) face, and rectangular for a (110) face, as shown in Figs. 8-10. Both the dark regions and the bright diffuse patterns rotate when the sample is rotated but stay in place when the sample is laterally moved, suggesting that the sample behaves as a directional reflector, and these image phenomena are caused by signal electrons being preferentially reflected at certain angles (Fig. 11).

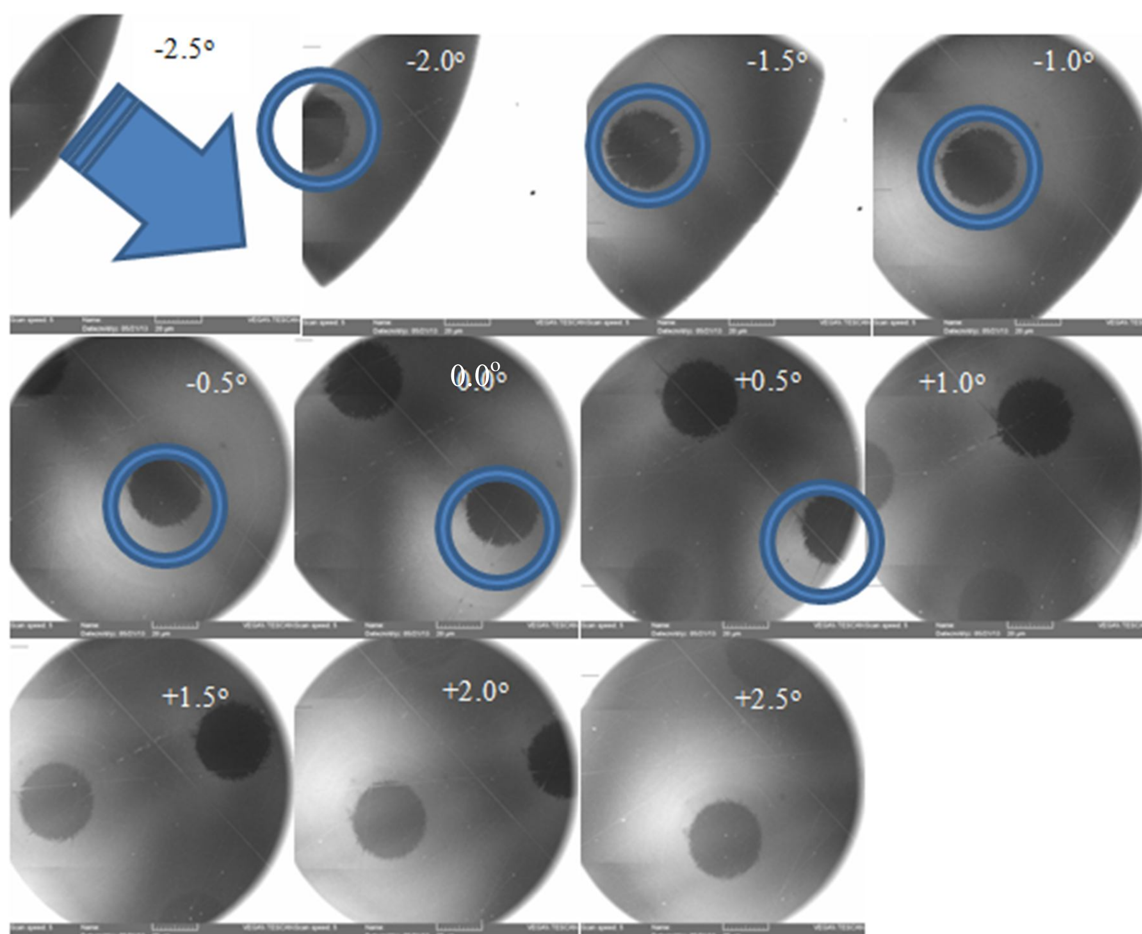

FIG. 11. A series of images showing the apparent movement of the dark regions in the image with the tilt of the sample. The tilt angle ranges from +2.5° to – 2.5° in steps of approximately 0.5 degrees. Both the dark regions and the bright diffuse patterns rotate with the sample but stay in place when the sample is laterally moved. The circle indicates one of the dark regions to show its movement with the tilt.

These phenomena seem to be consistent with electron channeling/diffraction, in which if the crystal is tilted or rotated the bands move as if fixed rigidly to the lattice but a translation of the crystal has no effect on the pattern, as the crystal symmetry is not changed. This seems to be related to phenomena seen in current image diffraction (CID), as described in Refs. [17, 18].

3.2. Experiment vs. Theory

At low energies, band structure effects play an important role, strongly modulating very-low-energy reflectivity [3]. Figure 12 shows EBSD maps of the normal and transverse directions for Cu polycrystalline. These maps were created by applying the Knapek and Pokorna (2015) technique to identify polycrystalline grain boundaries and assess the image signals in relation to electron impact energy.

It should be stressed that the brightness of grains in a polycrystalline material is not uniform, as shown in Fig. 12. Figure 12 depicts very-low-energy electron reflectivity signals from Cu polycrystalline with different grains oriented identically in the normal direction. These signals are averaged over the entire grain area, serving more or less as an illustrative example. Similar to single crystals shown in Figs. 8-10, the brightness distribution over the grain area also depends on the position of the grain in the field of view, changing with the azimuthal angle and the distance from the center of the field of view (Fig. 12).

Therefore, the averaged brightness cannot serve as a universal indicator, as other factors must be considered. This effect is most pronounced in crystallographic orientations close to fcc (111) orientation, in which the atomic planes facing the surface are the densest (Fig. 10).

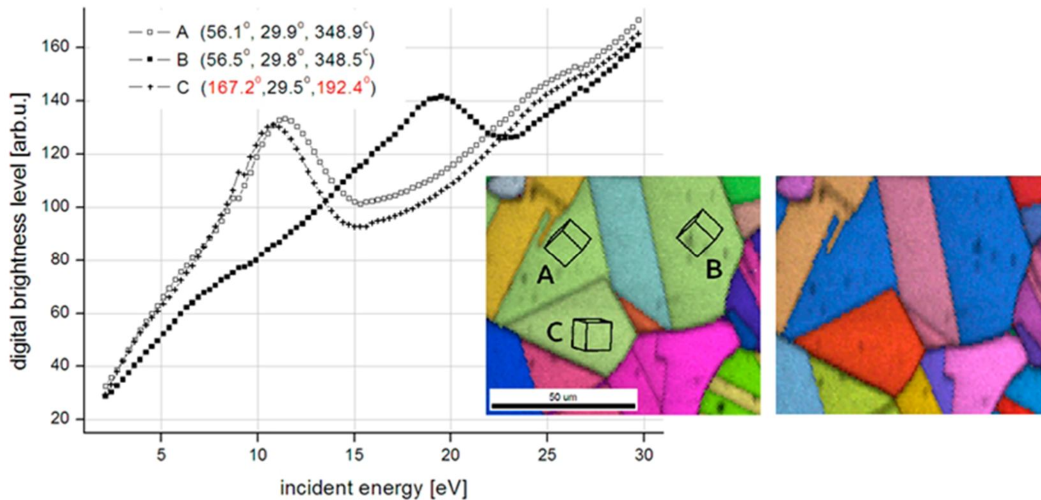

FIG. 12. Very-low-energy electron reflectivity signal from Cu polycrystalline (A, B, and C) grains oriented identically in the normal direction, as shown in the electron backscatter diffraction (EBSD) map on the left, but differently in the transversal direction (see the EBSD map on the right), i.e. rotated with respect to surface normal. The Euler angles of the respective grains, determined in another EBSD-equipped system, are shown in the graph on the left, as well as the corresponding SLEEM curves obtained in an ultra-high vacuum system.

Fig. 13 shows a comparison of very-low-energy electron reflectivity from Al single crystals of three basic orientations, as measured inside the darker spot in the center of the field of view. Each crystallographic orientation has different reflection intensity. For (110) fcc crystallographic orientations, the intensity is greater than for the other orientations in which the atomic planes facing the surface are the densest.

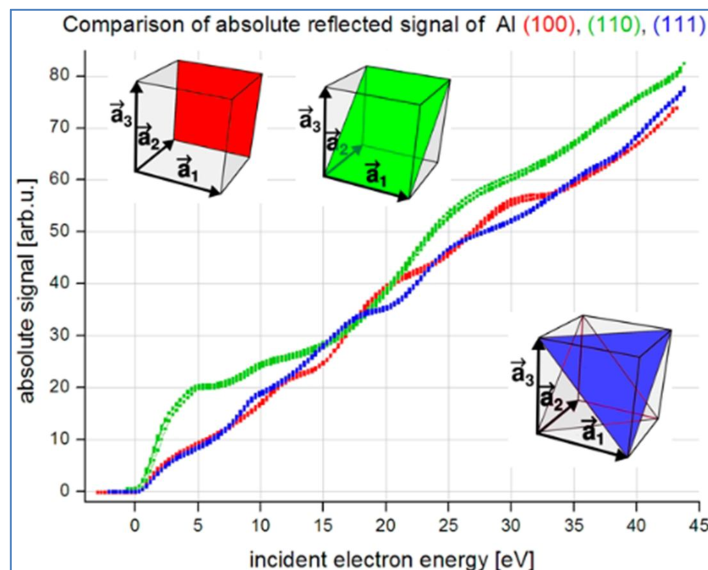

FIG. 13. A comparison of very-low-energy electron reflectivity from Al single crystals of three basic orientations, as measured inside the darker spot in the center of the field of view.

An example of one of the many measurements in the polycrystalline aluminum sample is shown in Fig. 14. It is evident that the background changes are a source of important deviation from the course of the expected reflectivity, especially in aluminum grains close to the (111) orientation, where there is a visible brightness gradient within larger grains. Generally speaking, Al (100) grains seem to be less affected, with (110) grains showing even fewer issues. This entire problem, however, might be amended by a moving stage and a stationary beam instead of a rocking mode beam scanning.

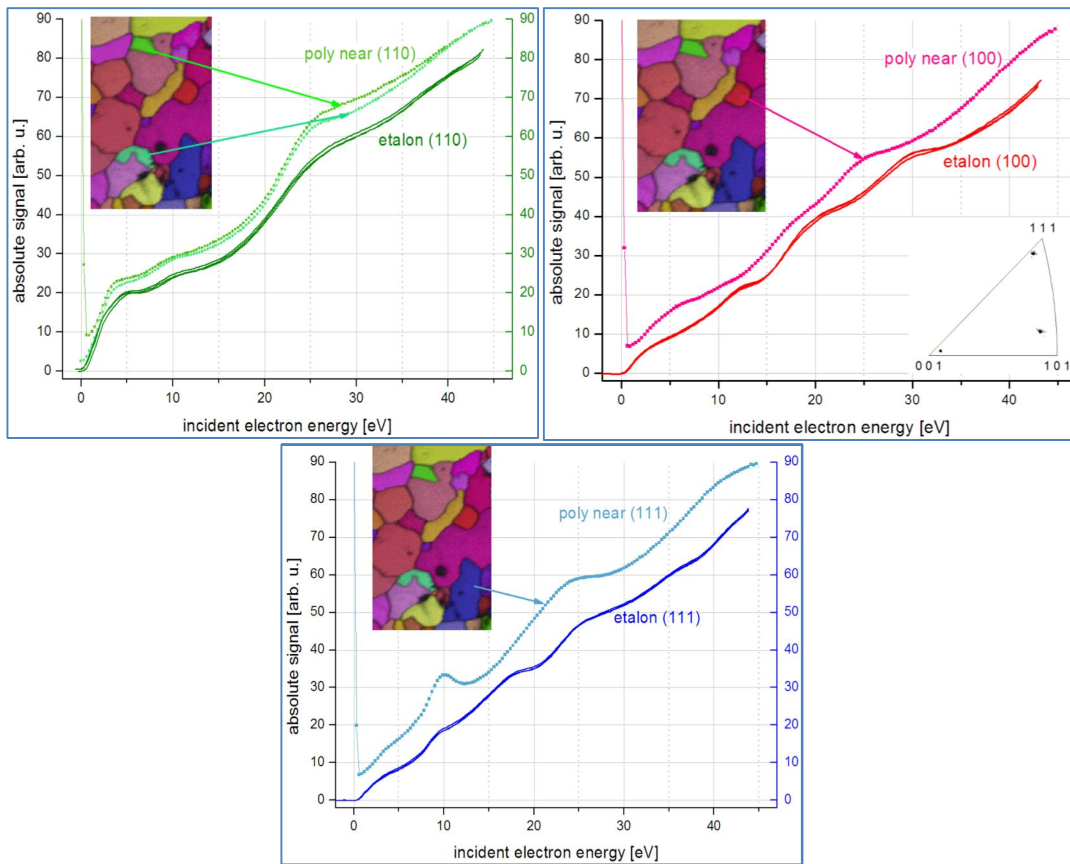

FIG. 14. Polycrystalline aluminum, a location with three grains close to the basic orientation. Comparison of the reflected signals of Al (100), Al (110), and Al (111).

The dark spots appearing in the images of polycrystalline grains in Fig. 14 are apparently artifacts of the chosen detection setup, in which a part of the signal electron bunch is strongly reflected in a preferred direction, disappearing in the BSE detector bore (Fig. 15).

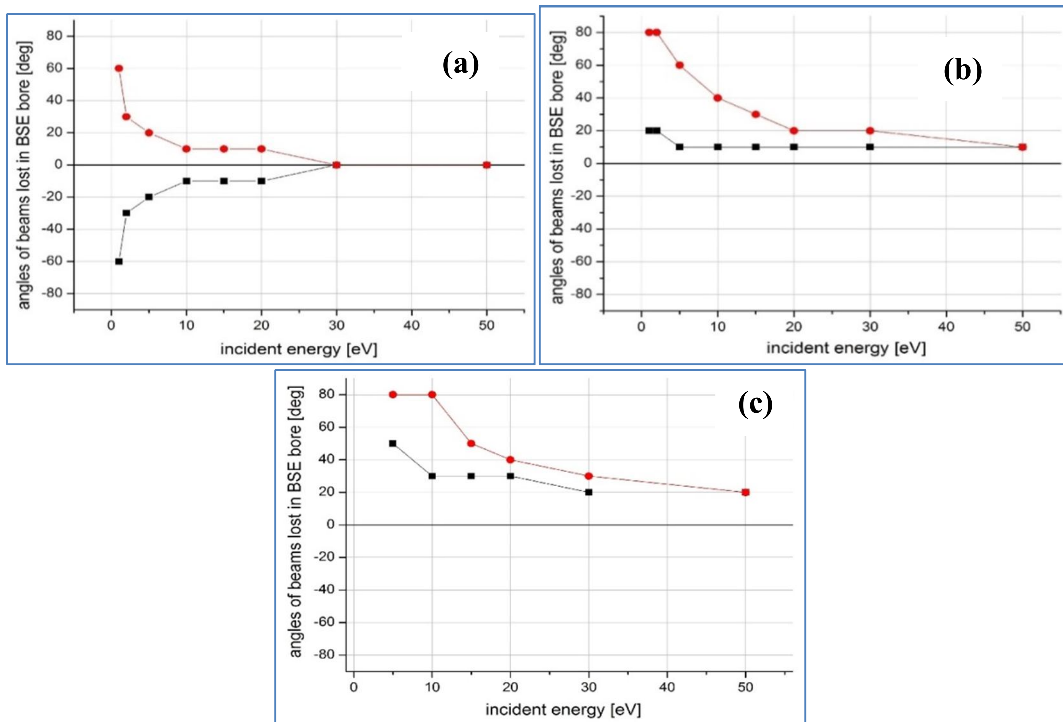

FIG. 15. An example of the angular range of signal electrons that are lost in the BSE bore. Three locations of beam incidence are considered: (a) center of field of view, (b) halfway to the edge, and (c) edge.

4. Theoretical Aspects

The observed phenomena are similar in nature to those acquired in current image diffraction (CID), as described in Refs. [17, 18]. This technique scans the beam with a wide incident angle sweep of ±2.5° to image the surface using sample current. In the SLEEM technique, it is the reflected signal that is collected, and the incident angle can reach up to 90° at very high immersion ratios (Fig. 11).

CID employs incident energies of 40-400 eV above the threshold for the emergence of diffracted beams, whereas the present technique goes as low as units of eV. CID can be used mainly to obtain information about the topmost layers (atomic layer distance, presence of adsorbates, etc.) or inner potential.

As mentioned by [17], the quantitative interpretation of CID patterns is complicated by the fact that in addition to elastically backscattered electrons, inelastically backscattered and secondary electrons also contribute to the measured current. Separation of the various contributions is problematic because their relative magnitudes are unknown. The same is true for the SLEEM setup shown in Fig. 1 because there is no energy filtering employed. However, for energies where contrast changes are caused by elastic backscattering, quantitative surface information may be extracted from the CID patterns in conjunction with theoretical calculations.

According to [4], backscattering does not necessarily have to occur particularly strongly at the lowest incidence of electron energies because of the weak electron-matter interaction and the significant effect of atomic potentials. According to the calculated data in Fig. 16 (left), Cu shows strong backscattering at the lowest energies in contrast to Al, however, this is reversed above 40 eV.

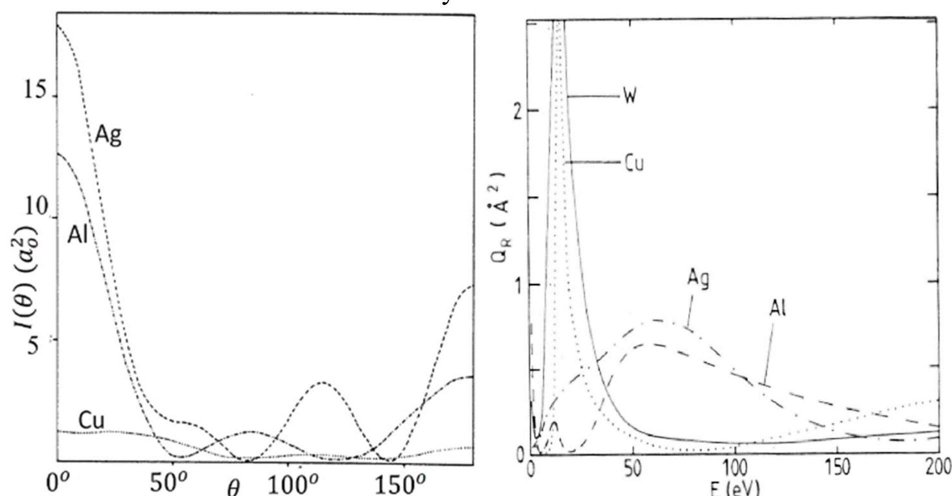

FIG. 16. *Left*: Calculated integral backscattering into a 30° cone around the backward direction. *Right*: Calculated scattering of electrons at E_{inc}= 50 eV from Ag, Al, and Cu into particular angles. Data taken from [4].

It's important to specify the exact influence of the band structure above E_{vac} and to determine the energy range over which this effect extends. It is also necessary to find out what the experimental vs. expected energy distribution in the signal is, either by absorbed current measurement or by the acquisition of the reflected signal in its entirety using a signal electron deflection setup.

Recording the angular anisotropy of the image signal can be facilitated by using a pixelated or segmented detector, or by broadening the signal electron bunch and recording its parts. The expected angular distribution is a matter of theoretical calculations that are far from definitive in the low-energy range, as depicted in Fig. 16 (right).

It might also be of interest to differentiate which depths contribute to specific angular distributions, as the sampled depths change, and the beam explores different depth ranges within the chosen incident energy bracket. This approach is similar to that used in the case of polymer blends as discussed in [19].

The incident beam intensity entering the sample varies with energy due to reflections on bandgaps in the band structure above the vacuum level, as shown in Ref. [4]. The angle of incidence of the beam, however, is much larger than the scan angle due to the cathode lens and

depends on incident beam energy and the intensity of the decelerating field. The angle of incidence is also influenced by any optical misalignment. This should be considered when assessing phenomena dependent on the direction of the incoming beam. Channeling through sparse directions in the crystalline structure also plays a role here, as does diffraction on various crystal planes.

Since the signal is not captured in its entirety, it is essential to determine the incidence angles throughout the field of view to find out what portion of the signal gets lost in the bore.

Conclusions

The present work has mapped the dependence of very-low-energy electron reflectivity (0-30 eV) on the energy and angle of incident electron impinging on the surface of crystalline metals (Al and Cu). The dependence seems to be consistent with the electron channeling and diffraction principles, where the crystal behaves as a directional reflector. If the crystal is tilted or rotated, the bands move as if fixed rigidly to the lattice. A translation of the crystal has no effect on the pattern, most likely because the crystal symmetry is not changed. This seems to be related to phenomena seen in current image diffraction.

The present research demonstrates that the measured reflected signal curves from SLEEM are specific for each crystal orientation. This opens the door for identifying the grain orientation in polycrystals using reflectance curves as a fingerprint.

In practical applications, this methodology could be applied to investigate how areas with different oxidation states behave, which holds significance for industries like steel manufacturing.

Acknowledgments

The research described in this article was financially supported by the Czech Academy of Sciences (RVO:68081731).

References

[1] Jaklevic, R.C. and Davis, L.C., Phys. Rev. B, 26 (10) (1982) 5391.

[2] Herlt, H.J. and Bauer, E., Surf. Sci., 175 (2) (1986) 336.

[3] Bauer, E., Rep. Prog. Phys., 57 (1994) 895.

[4] Bauer, E., Surf. Rev. Lett., 5 (06) (1998) 1275.

[5] Tromp, R.M., IBM J. Res. Dev., 44 (2000) 503.

[6] Fadlallah, M.M., Schuster, C., Schwingenschlögl, U., Wunderlich, T. and Sanvito, S., J. Phys.: Condens. Matter, 21 (31) (2009) 315001.

[7] Assa'd, A.M.D., Jordan J. Phys., 12 (1) (2019) 37.

[8] Assad, A.M.D. and El-Gomati, M.M., Scanning Microsc., 12 (1998) 185.

[9] El-Gomati, M.M., Walker, C.G.H., Assa'd, A.M.D. and Zadrazil, M., Scanning, 30 (2008) 2.

[10] Walker, C.G.H., El-Gomati, M.M., Assa'd, A.M.D. and Zadražil, M., Scanning, 30 (2008) 365.

[11] Read, M.N., Phys. Rev. B, 75 (19) (2007) 193403.

[12] Kasll, J., Mikmeková, Š. and Jandová, D., IOP Conf. Series: Mater. Sci. Eng., 55 (2014) 012008.

[13] Müllerová, I. and Frank, L., Adv. Imaging Electron Phys., 128 (2003) 310.

[14] Müllerová, I. and Frank, L., Microchim. Acta, 114 (1) (1994) 389.

[15] Pokorná, Z., PhD Thesis, Faculty of Science, Masaryk University, Brno, (2012), Czech Republic

[16] Musket, R.G., McLean, W., Colmenares, C.A., Makowiecki, D.M. and Siekhaus, W.J., Appl. Surf. Sci., 10 (2) (1982) 143.

[17] Bargeron, C.B., Nall, B.H. and Jette, A.N., Surf. Sci., 120 (2) (1982) L483.

[18] Kawamura, T., Surf. Sci., 152 (1985) 43.

[19] Masters, R.C., Pearson, A.J., Glen, T.S., Sasam, F.C., Li, L., Dapor, M., Donald, A.M., Lidzey, D.G. and Rodenburg, C., Nat. Commun., 6 (2015).